

PAPER • OPEN ACCESS

On the modeling of roughness effects on the transition of von Kármán boundary-layer flow

To cite this article: PYAGSYapa et al 2025 Fluid Dyn. Res. 57 055505

View the article online for updates and enhancements.

You may also like

- <u>Study on Gradation and Performance of Cold Patch Asphalt Mixtures</u>
 Li Qiang, Liu Feiyi, Luo Xiao et al.
- Understanding Temperature Stability of Surface Cation Dopants on LSCF Electrodes
 Sophie Coppieters 't Wallant, Filip Grajkowski, Bill Liu et al.
- Organosilicon-Based Electrolytes with Superior Thermal and Electrochemical Stability to Enable High Energy Lithium Ion Batteries

Monica Lee Usrey, Adrian Pena Hueso, Michael Pollina et al.

Fluid Dyn. Res. 57 (2025) 055505 (22pp)

https://doi.org/10.1088/1873-7005/ae0af3

On the modeling of roughness effects on the transition of von Kármán boundary-layer flow

P Y A G S Yapa¹, Paul Griffiths², Stephen J Garrett² and Peter J Thomas^{1,*}

- ¹ Fluid Dynamics Research Centre, School of Engineering, University of Warwick, Coventry, United Kingdom
- ² School of Engineering and Innovation, Aston University, Birmingham, United Kingdom

E-mail: P.J.Thomas@warwick.ac.uk

Received 12 May 2025; revised 20 August 2025 Accepted for publication 23 September 2025 Published 9 October 2025

Communicated by Dr Benoit Pier



Abstract

Laminar-turbulent boundary-layer transition over rough rotating disks is addressed by means of linear-stability analysis. Computational data from two frequently used roughness-modeling approaches are obtained as input data for the stability analysis. It is demonstrated that the data arising from the two different approaches are not compatible with each other. Nevertheless, the stability analysis predicts postponed transition for both approaches. Two main conclusions emerge. Firstly, a theoretical study is required to establish which particular characteristics of the input data set result in the linear-stability analysis predicting postponed transition. Secondly, to guide future simulations an experimental study is essential to determine which one of the roughness-modeling approaches, if either, can produce data in agreement with measurements.

Keywords: rotating-disk flow, boundary-layer transition, roughness modeling, linear-stability analysis

Original Content from this work may be used under the terms of the Creative Commons Attribution 4.0 licence. Any further distribution of this work must maintain attribution to the author(s) and the title of the work, journal citation and DOI.

Author to whom any correspondence should be addressed.

1. Introduction

The current paper addresses issues associated with the effects of surface roughness on the laminar-turbulent transition of the boundary-layer flow over a rotating disk. The disk is spinning within an infinite, ambient fluid that is at rest far above the disk surface. This flow configuration was first analyzed theoretically by von Kármán (1921) and it is now commonly referred to as von Kármán flow. Its associated boundary layer is representative of a class of boundary layers widely encountered in connection with rotating components of machinery or the flow over highly swept wings (see Wimmer 1988, Lingwood and Alfredsson 2015, Alfredsson *et al* 2024).

Two roughness-modeling approaches have been used by ourselves (Cooper et al 2015, Garrett et al 2016) and numerous authors (e.g. Alveroglu et al 2016, Alqarni et al 2019, Alveroglu 2020, 2021, Thomas et al 2020, 2023, Al-Malki et al 2022, Khan et al 2022a, 2022b, Igra et al 2024) in recent years to study the effects of simple geometric roughness patterns on the laminar-turbulent transition of the von Kármán boundary-layer. The first of these two approaches models roughness in terms of prescribing partial slip on the disk surface. This approach dates back as far as 1823 (Navier 1823). The partial-slip route appears to have been first applied in the context of the von Kármán boundary layer by Miklavčič and Wang (2004). We first adopted the methodology in Cooper et al (2015). The alternative approach is to model roughness directly by prescribing particular surface structures. That methodology was used for the von Kármán boundary layer by Yoon et al (2007) and we applied it for the first time in Garrett et al (2016). In Cooper et al (2015) we introduced the abbreviations MW and YHP for, respectively, the partial slip (Miklavčič and Wang 2004) and the direct approach Yoon et al (2007), subsequent authors adopted the nomenclature (see Alveroglu et al 2016, Algarni et al 2019, Alveroglu 2020, 2021, Thomas et al 2020, 2023, Al-Malki et al 2022, Khan et al 2022a, 2022b, Igra et al 2024).

Due to the different nature of the MW and the YHP approach, a meaningful comparison of results produced with the two methodologies is not straightforward. That is, because both use different, unrelated roughness-control parameters. In Cooper *et al* (2015), Garrett *et al* (2016) we used the MW and the YHP approach to model the effects of roughness patterns of concentric grooves for the rotating-disk boundary layer. However, the data in Cooper *et al* (2015), Garrett *et al* (2016) were not suitable for a direct comparison to one another. Nevertheless, both approaches predicted postponed transition. Here we revisit the roughness patterns of concentric grooves but for particular simulation conditions that enable conclusions that were not possible on the basis of the data in Cooper *et al* (2015), Garrett *et al* (2016).

2. Rotating-disk flow

The three-dimensional flow structure of the boundary-layer flow over a rotating disk is illustrated in figure 1. For the theoretical analysis the disk is assumed to be of infinite radial extent (see, for instance, von Kármán 1921, Owen and Rogers 1989). The three velocity components are the azimuthal (G), radial (F) and axial (H) flow components. These velocity components constitute an exact similarity solution to the Navier–Stokes equation (von Kármán 1921).

The nature of the azimuthal flow component arises from the requirement that no-slip has to be satisfied on the surface of the rotating disk, while the fluid far above the disk is stationary. The radial component is a consequence of no-slip together with the action of the centrifugal force on the fluid within the boundary layer and stationary fluid far above. Note that this constellation necessitates the existence of an inflexion point on the radial flow profile at

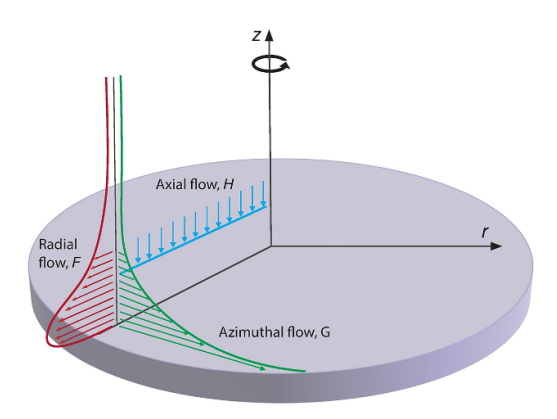


Figure 1. Boundary-layer velocity components of rotating-disk flow.

some height above the disk surface. The radial flow is commonly referred to as the crossflow component because it is aligned at a right angle to the azimuthal component. The axial flow component arises in connection with the radial component. Mass-conservation necessitates its existence to replace the liquid that is being transported radially outwards.

The transition of the rotating-disk boundary layer is associated with different stationary and travelling instability modes (Lingwood and Alfredsson 2015, Alfredsson *et al* 2024). The mode that has received most attention is the stationary Type I crossflow instability. That mode arises as a consequence of the existence of the inflexion point on the profile of the radial flow-velocity component (Lingwood and Alfredsson 2015, Alfredsson *et al* 2024). The existence of the inflexion point on the crossflow component is a crucial aspect shared by all boundary layers with such a crossflow component. The Type I mode is responsible for the laminar-turbulent transition of the rotating-disk boundary layer and other boundary layers with a crossflow component. It has been identified as giving rise to the characteristic spiral vortices, developing in the transition zone over the disk (Mack 1985). These spiral vortices were first visually documented in Gregory *et al* (1955), together with corresponding vortices on swept wings.

The theoretical aspects associated with the derivation of the similarity solution for the boundary-layer velocity profiles G, F and H, following von Kármán's (1921) original publication, and the details of the linear-stability theory for these profiles are standard and have been summarized numerous times in the past. Therefore, we will not reiterate the lengthy mathematical details here. We kindly ask readers to access the comprehensive literature available (see Owen and Rogers 1989, Cooper *et al* 2015, Lingwood and Alfredsson 2015, Garrett *et al* 2016, Yapa 2023, Alfredsson *et al* 2024). Here only the most fundamental aspects required to follow the current discussion are outlined.

For the mathematical description of the rotating-disk flow geometry it is natural to employ a cylindrical polar coordinate system r, θ, z with respective steady-flow components v_r, v_θ, v_z . The flow is assumed to be rotationally symmetric, such that there exists no θ -dependence.

The characteristic length scale of the problem is given by the order of magnitude of the boundary-layer thickness

$$d = \sqrt{\nu/\Omega} \quad , \tag{1}$$

where ν is the kinematic viscosity of the fluid and Ω is the rotational velocity of the disk. Therefore, the non-dimensional height above the disk is given by

$$\zeta = \frac{z}{\sqrt{\nu/\Omega}} \ . \tag{2}$$

The nondimensional velocity components are

$$F(\zeta) = \frac{v_r}{\Omega r}, \quad G(\zeta) = \frac{v_\theta}{\Omega r}, \quad H(\zeta) = \frac{v_z}{(\Omega \nu)^{\frac{1}{2}}} \quad , \tag{3}$$

and the Reynolds number is defined as

$$Re = \sqrt{\frac{\Omega r^2}{\nu}} . {4}$$

Substituting equation (1) into equation (4) yields Re = r/d. Thus, the Reynolds number corresponds to the nondimensional distance from the center of the disk.

The Reynolds number is related to the azimuthal disturbance wavenumber, β , and the number of spiral vortices, n, developing in the rotating-disk boundary layer during transition by

$$\beta = \frac{n}{Re} \ . \tag{5}$$

3. Roughness models

The MW and the YHP approach proceed by initially finding the roughness-modified base-flow profiles for $F(\zeta)$, $G(\zeta)$, $H(\zeta)$ (see Cooper *et al* 2015, Garrett *et al* 2016). To that end two separate codes are used. These modified velocity profiles are then subjected to a linear-stability analysis conducted by means of a third, separate code. For what lies ahead it is crucial to appreciate that the linear-stability code represents a separate entity from the other two codes used to produce the modified base profiles. That is, the linear-stability code does not know whether any particular set of roughness-modified input velocity profiles originated from the MW or the YHP approach.

Based on the roughness-modified input velocity profiles the linear-stability code yields neutral-stability curves for the flow disturbances as a function of the Reynolds number. In the context of the stability analysis note that we are considering stationary instability modes only. For smooth disks our computational base-flow velocity profiles and the neutral-stability curves produced by our neutral-stability code for the stationary modes agree with the well-established results by, respectively, von Kármán (1921) and Malik (1986).

For the MW approach (Cooper *et al* 2015) the roughness-control parameter is an ad-hoc slip factor introduced to ensure that the flow speed on the disk surface is non zero. For the YHP approach (Garrett *et al* 2016) surface undulations on the disk are prescribed with the no-slip condition being satisfied on the disk surface. The roughness control parameter for the YHP approach is the wavelength-to-pitch ratio. There exists no natural physical relation between the slip factor and the wavelength-to-pitch ratio within the current mathematical framework of the MW and the YHP methodology.

The MW and the YHP approach provide two options to make data comparable. These are to either attempt making the roughness-modified mean base flow velocity profiles equal or to adjust the two roughness-modeling parameters such that the volumetric flow rate through the system is equal. It will be seen (cf discussion of figures 4–6) that making the three corresponding flow velocity components equal is impossible. Therefore, the only option for a comparison

is to adjust the roughness modeling parameters such that they result in the same volumetric through flow. That constellation is evidently not ideal. Because, as will be seen, when the flow rates match the corresponding velocity profiles differ. Nevertheless, the main conclusions that will emerge are independent of that shortcoming.

The axial (downward) mass flow rate \dot{m}_{ζ} at height ζ is

$$\dot{m}_{\zeta} = \int_{0}^{r=r_0} \int_{\theta=0}^{\theta=2\pi} \rho H(\zeta) r \, \mathrm{d}r \, \mathrm{d}\theta , \qquad (6)$$

where the upper limit $r = r_0$ of the integral in equation (6) represents any particular radial extent of the flow field to be considered. In practice, for the case of a finite disk, this would be the disk radius. Using 3(c), and considering that one obtains the total inflow rate, $\dot{m}_{\rm in}$, when $\zeta \to \infty$ this gives

$$\dot{m} = \frac{\dot{m}_{\rm in}}{C} = H_{\infty} \quad . \tag{7}$$

The constant C in equation (7) is

$$C = \pi \rho r^2 \left(\Omega \nu\right)^{\frac{1}{2}} , \tag{8}$$

and the notation $\dot{m} \equiv H_{\infty}$ is used as a reminder that it represents the total incoming mass-flow rate. The cut off $\zeta=20$ was used to compute \dot{m} from the data sets since the flow rate remains invariant for larger ζ values. Adjusting \dot{m} to be equal for the YHP and the MW approach is the criterion for which data will be compared.

The YHP approach assumes rotational symmetry. It can, therefore, only model roughness in the radial direction. Undulations in the radial direction, under the condition of rotational symmetry, implies that the simulations correspond to a disk with concentric grooves of a particular cross-sectional shape. The cross-sectional shape examined here, and in Garrett *et al* (2016), is given by

$$s(r) = \delta \cos(2\pi r/\gamma) \quad , \tag{9}$$

where δ is the undulation amplitude and γ is the pitch of the roughness. The roughness-control parameter for the YHP approach is the amplitude-to-pitch ratio

$$a = \delta/\gamma$$
 . (10)

The base-flow profile resulting from the YHP approach that is being submitted to the stability analysis is then taken as a spatial, radial average over one period of roughness (see Garrett *et al* 2016).

The MW approach can, in principle, model roughness in the radial as well as in the azimuthal direction by introducing separate slip factors for each of the two velocity components. Results for various combinations of radial and azimuthal slip factors can be found in Cooper *et al* (2015). To define a flow that corresponds to the concentric grooves of the YHP approach only a slip factor for the radial velocity component must be used here as a control parameter for the MW approach. The azimuthal flow velocity when using the MW approach remains to satisfy the no-slip boundary condition.

Navier's partial-slip approach (Navier 1823, Miklavčič and Wang 2004) assumes that the velocity tangent to the surface is proportional to the wall shear stress. We follow the notation of Miklavčič and Wang (2004) and introduce partial slip for the radial velocity component in terms of a generalization of Navier's partial slip condition as

$$v_r|_{z=0} = N\rho\nu \left. \frac{\partial v_r}{\partial z} \right|_{z=0} . \tag{11}$$

Table 1. Data YHP appoach.

m	а	Re_c	n	ζ_I	F_{I}	F_I'
0.8845	0	286.3	22.2	1.82	0.132	-0.0754
0.9114	0.08	302.4	20.9	1.97	0.125	-0.0651
0.9413	0.12	327.7	20.2	2.14	0.118	-0.0556
0.9779	0.16	367.9	20.0	2.33	0.111	-0.0462
1.0178	0.20	422.3	20.2	2.52	0.104	-0.0378

Table 2. Data MW approach.

m	λ	Re_c	n	ζ_I	F_I	F_I'
0.8845	0	286.3	22.2	1.82	0.133	-0.0754
0.9101	0.10	316.64	27.5	1.67	0.141	-0.0825
0.9386	0.23	371.05	35.9	1.53	0.152	-0.0916
0.9747	0.44	488.32	53.6	1.36	0.169	-0.1054
1.0146	0.77	741.2	92.9	1.20	0.190	-0.1232

In equation (11) N is referred to as the slip coefficient. Note that dimensional homogeneity requires the dimensions of N to be Length² × Time/Mass. The dimensionless roughness-control parameter for the MW approach is then defined as

$$\lambda = N\rho\sqrt{\nu\Omega} \quad , \tag{12}$$

Using these definitions yields

$$F(0) = \lambda F'(0) \quad , \tag{13}$$

the prime denotes differentiation with respect to ζ .

4. Results

Tables 1 and 2 summarize, respectively, relevant data for the simulations with the YHP and the MW approach. Included in the tables are the values of the two control parameters $a = \delta/\gamma$ (YHP) and λ (MW) that lead to equal mass-flow rate, \dot{m} .

To obtain sets of results for equal mass flow rate for both computational approaches the value of either a or λ was pre-selected. The corresponding set of data for the other approach was then obtained by successive computational runs, changing the relevant control parameter by small increments until the mass-flow rates for both approaches agreed to one another to within an accuracy of less than one percent.

Also included in tables 1 and 2 are some values of quantities arising in the context of the discussion further below. These are the critical Reynolds number Re_c for the Type I instability mode, the number n of spiral vortices developing above Re_c , the height ζ_I of the inflexion point of the radial flow velocity profile over the disk, as well as the radial flow speed, F_I , and its ζ -derivative F_I' , in the inflexion point. These data will be referred to in the remainder where relevant.

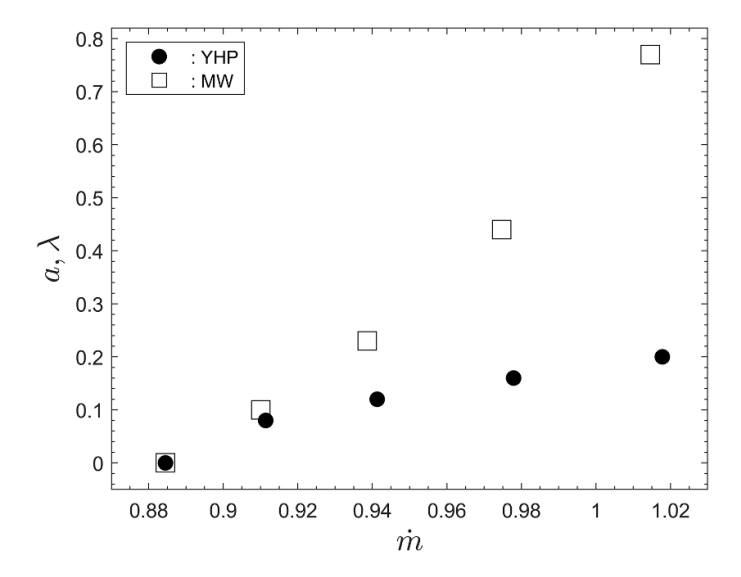


Figure 2. The roughness parameters, a for the YHP approach and λ for the MW approach, as a function of the mass-flow rate \dot{m} .

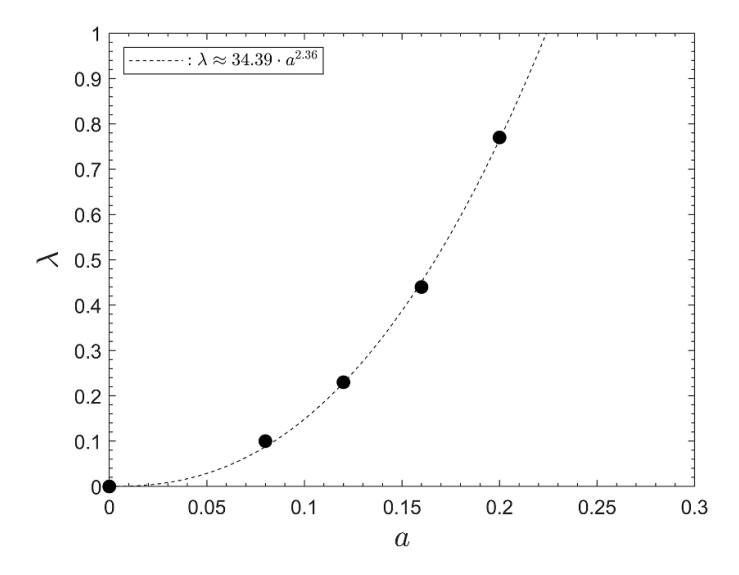


Figure 3. Roughness parameter a of the YHP approach as a function of the roughness parameter λ for the MW approach.

4.1. Roughness correspondence

Figure 2 displays a and λ as a function of the mass-flow rate \dot{m} . Recall that increasing \dot{m} represents increasing roughness. It can be seen that both parameters increase nonlinearly with the mass-flow rate. An interesting feature being that a increases faster than linearly with \dot{m} , while the opposite is the case for λ .

Figure 3 depicts the slip factor λ (MW) as a function of the amplitude-to-pitch ratio a (YHP), under the condition that both produce the same mass-flow rates, \dot{m} . While the data

displayed only relate to the rotating-disk flow it is interesting to see the nonlinear relationship between the two parameters. The data can be summarized in terms of a least-squares fit given by $\lambda = 34.4 \cdot a^{2.36}$.

4.2. Velocity profiles

Figures 4–6 display, respectively, the radial, azimuthal and axial velocity component of the flow over the rotating disk. In each of the three figures part (a) contains the results based on the YHP approach while (b) shows the results for the MW approach. Recalling that all data were obtained under the condition that roughness for both approaches results in equal mass-flow rates through the system. The black dots superposed onto the velocity profiles in figures 4(a) and (b) identify the location of the inflexion point on each of the radial velocity profiles. The shift of the location of the inflexion point will be discussed in section 4.3.

Reference to figure 4(a) reveals that in the region $\zeta \lesssim 1.8$ the radial velocity for the YHP approach decreases with increasing roughness, relative to the corresponding velocity for the smooth disk. The opposite is the case for the MW approach in figure 4(b). It is, therefore, impossible to adjust parameters such that the velocity profiles for the MW and the YHP approach match. Corresponding comments apply to the azimuthal velocity component in figure 5 and the axial velocity component in figure 6. Several similar examples of incompatible scaling behaviour will be observed in the remainder.

4.3. Inflexion point

It was discussed in section 2 that laminar-turbulent transition of the von Kármán boundary, and other boundary-layers with a crossflow component, is due to the Type I instability mode and that this mode arises from the inflexion point on the radial flow velocity F (see Lingwood and Alfredsson 2015, Alfredsson *et al* 2024). It is, therefore, interesting to investigate the characteristics of the inflexion point under the condition that the YHP and the MW approach result in equal mass-flow rates.

The location of the inflexion point on the radial flow-velocity component is identified in figures 4(a) and (b) by the black dots superposed onto the velocity profiles. The associated height (ζ_I) of the inflexion point above the disk surface and the radial velocity component (F_I) at that height are displayed in, respectively, figures 7(a) and (b) as a function of the mass-flow rate (\dot{m}). In both figures the full, black circles are the results obtained from the YHP approach, while the open squares represent the data for the MW approach. Since the mass-flow rate increases for both approaches with the relevant roughness-control parameter (cf tables 1 and 2) the data points for all data sets in figures 7(a) and (b) correspond to increasing roughness levels from left to right.

Figure 7(a) reveals that for the YHP approach the location of the inflexion point moves away from the disk surface for increasing roughness levels, while the opposite is the case for the MW approach. Similarly figure 7(b) shows that the radial flow velocity component at the location of the inflexion point decreases with increasing roughness level for the YHP approach, while the trend is reversed for the MW approach. Moreover, while the data from the YHP approach for ζ_I in figure 7(a) lie above those for the MW approach the situation is reversed for the velocity F_I in figure 7(b). Thus, the location and velocity data for the inflexion point display entirely opposing behaviour for both approaches.

Figures 8(a) and (b) display results for the ζ -derivative, F'_I , of the radial flow-velocity component. In figure 8(a) the derivative is displayed as a function of the mass-flow rate \dot{m} while figure 8(b) shows it as a function of the associated velocity F_I at the inflexion point. Similar

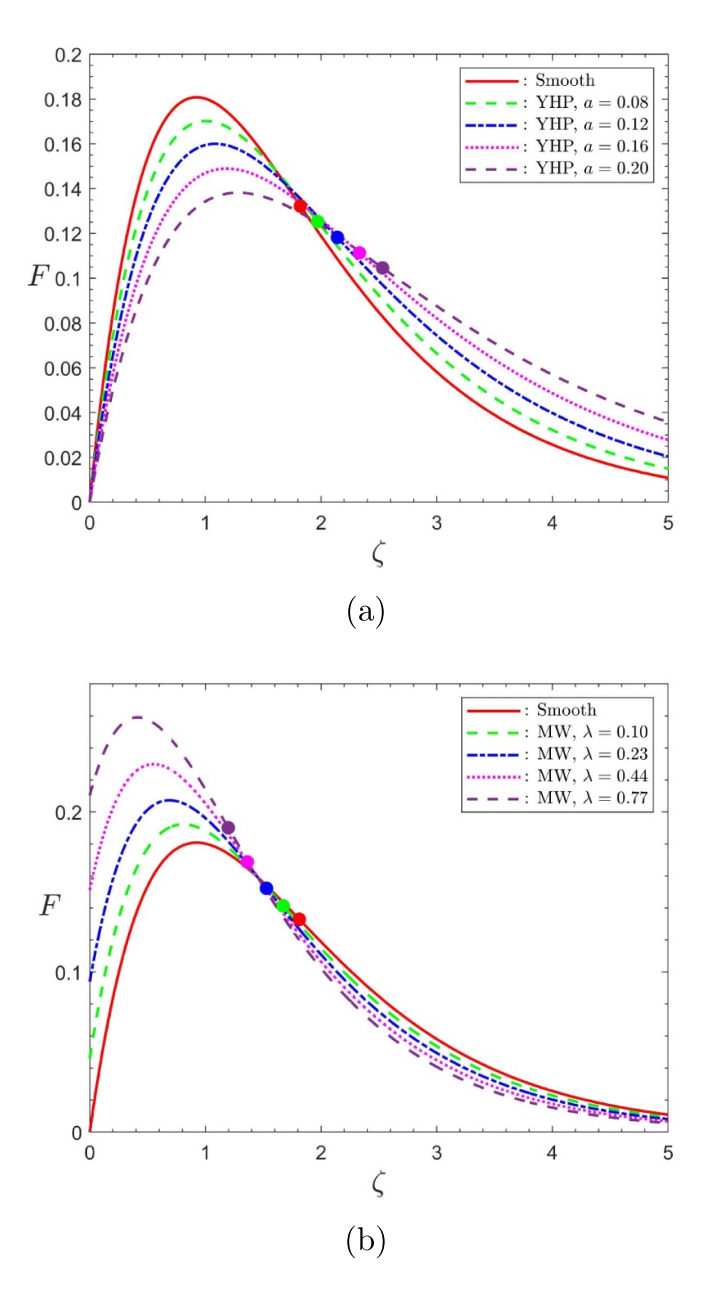


Figure 4. Radial flow velocity, F, as a function of the nondimensional height, z, above the disk surface. (a) YHP approach, (b) MW approach.

to figure 7 the velocity gradient F'_I in figure 8(a) displays opposing trends under the YHP and the MW approach.

Regarding the data for the gradient F_I' as a function of F_I in figure 8(b) note that the two overlapping data points, just above $F_I \approx 0.13$, represent the results for the smooth disk, obtained from the two different computational codes for the YHP and the MW approach. Data for the

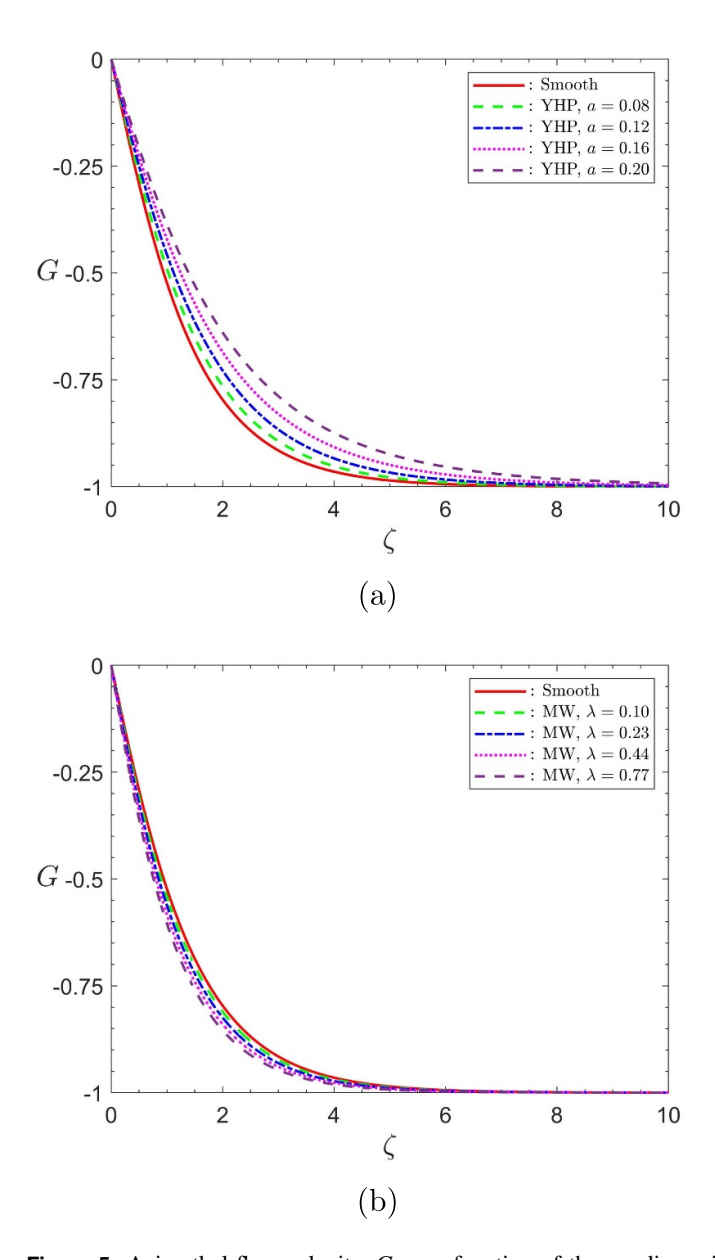


Figure 5. Azimuthal flow velocity, G, as a function of the nondimensional height, ζ , above the disk surface. (a) YHP approach, (b) MW approach.

YHP approach for successively decreasing F_I -values, below $F_I \approx 0.13$, correspond to increasing roughness levels. For the MW approach successively increasing F_I -values above $F_I \approx 0.13$ correspond to increasing roughness level. Thus, again opposing trends are observed. While increasing roughness in the YHP approach leads to an increased gradient F_I' the opposite is the case for the MW approach. Nevertheless, it is interesting to note that the data of both individual sets of results display a linear dependence of F_I' on F_I , and with only slightly different gradients $\mathrm{d}F_I'/\mathrm{d}F_I$.

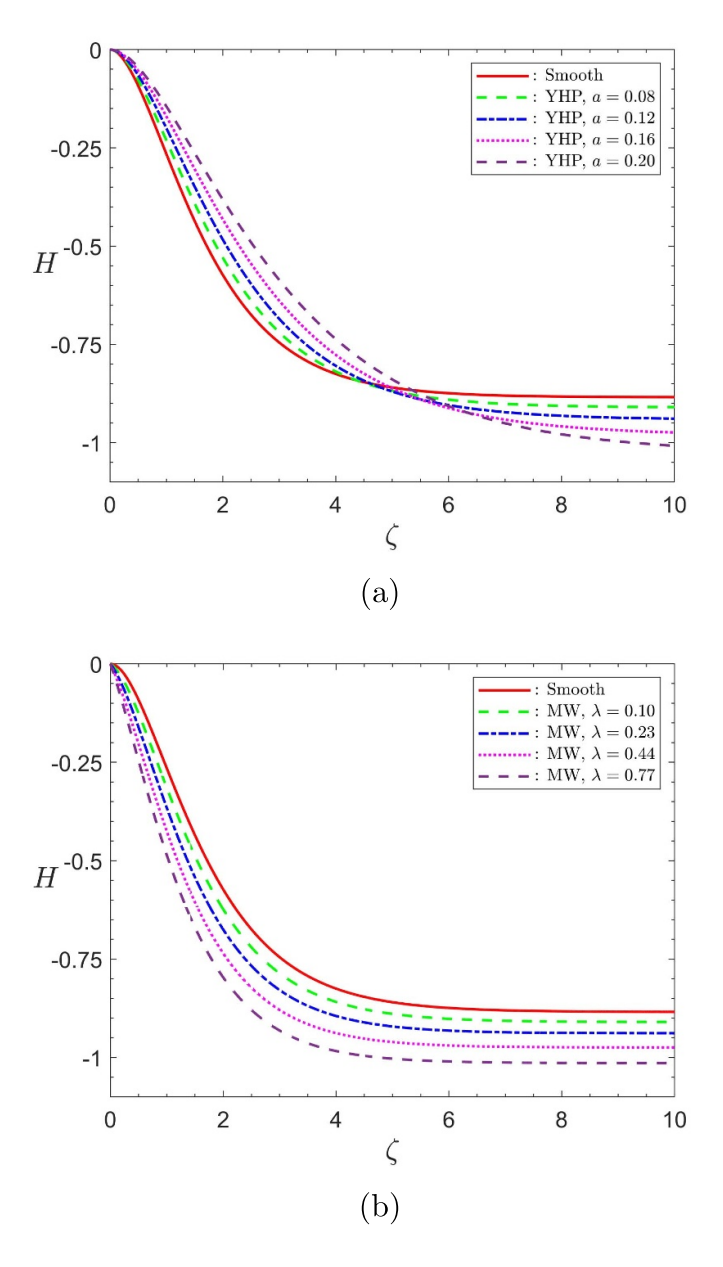


Figure 6. Axial flow velocity, H, as a function of the nondimensional height, ζ , above the disk surface. (a) YHP approach, (b) MW approach.

4.4. Neutral stability curves

Figures 9(a) and (b) display the neutral stability curves for increasing roughness levels, for the YHP and the MW approach, respectively. The figure shows the wavenumber, α_r , of the most unstable radial mode as a function of the Reynolds number Re. The $\alpha-Re$ combinations enclosed by the curves represent unstable conditions while combinations outside of the enclosed regions represent stable conditions. As is well known, the top lobe on the neutral

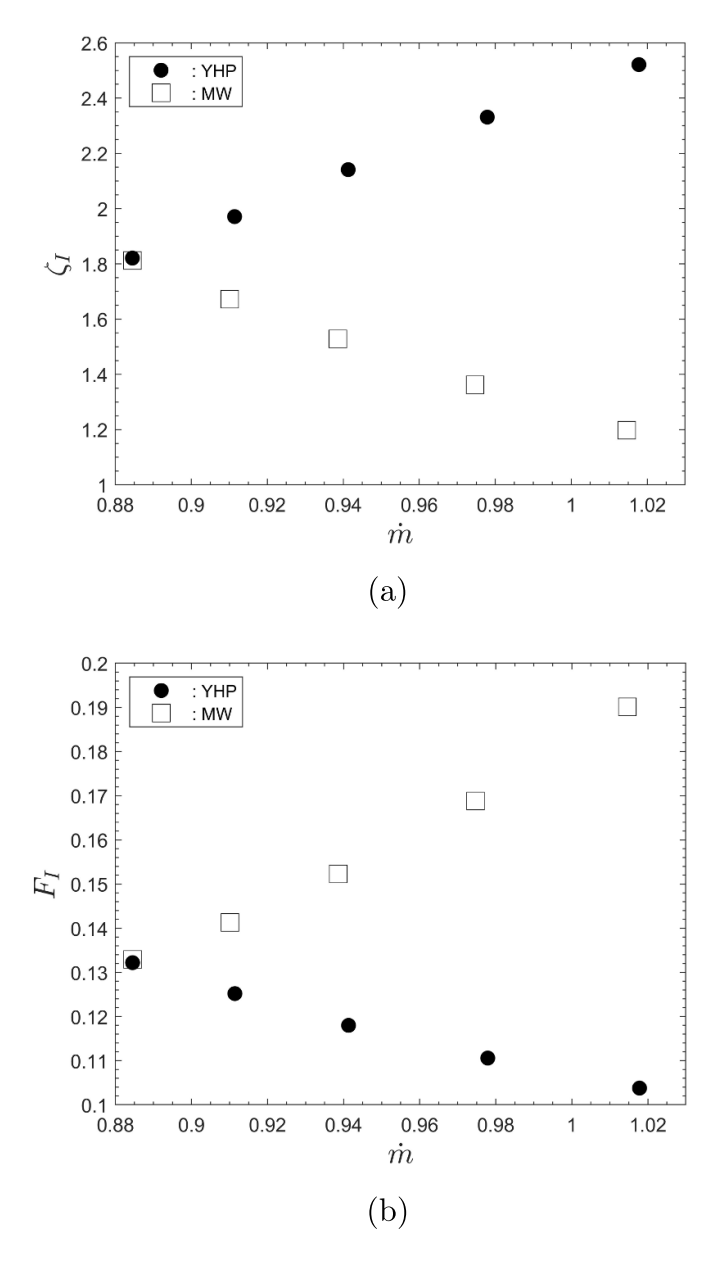


Figure 7. The (a) height of the inflexion point above the disk, ζ_I and the (b) radial flow velocity at the inflexion point, F_I , as a function of the mass-flow rate \dot{m} .

stability curves in figures 9(a) and (b) represents the Type I instability mode while the smaller bottom lobe corresponds to the Type II mode.

Figure 9 reveals that, as in Cooper et al (2015), Garrett et al (2016), the Type I mode is shifted towards higher Reynolds number by increasing roughness levels, for both the YHP

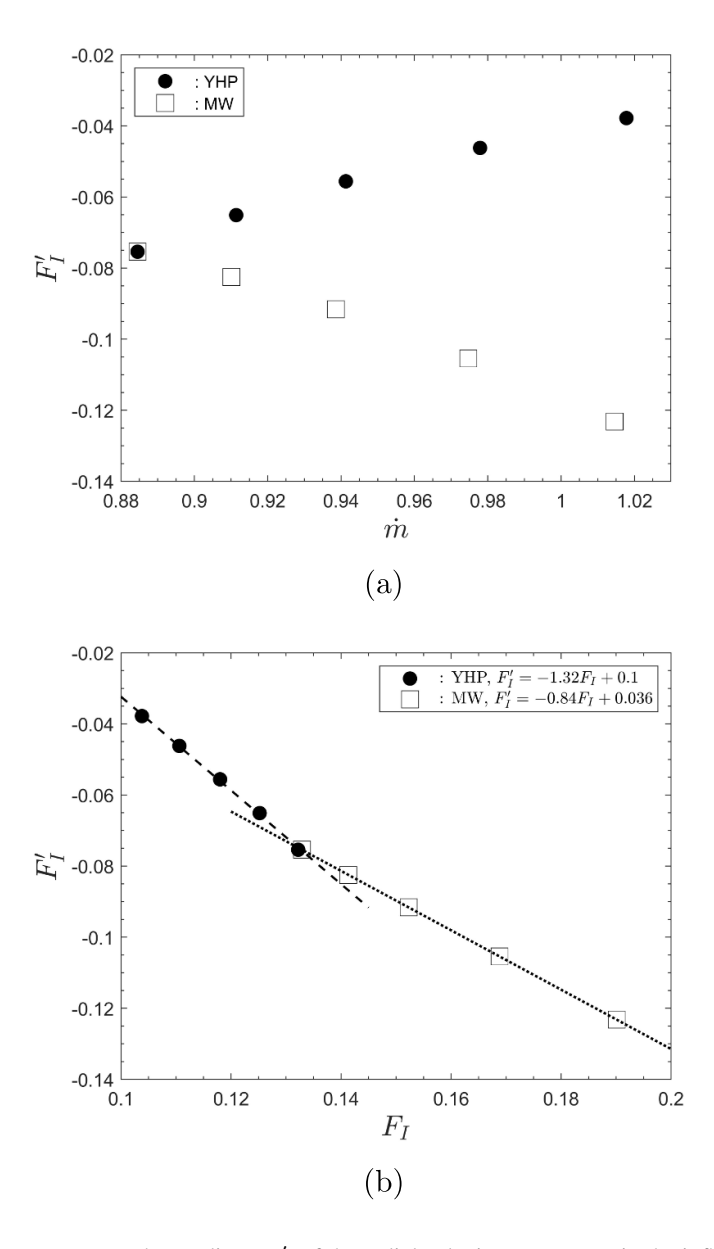


Figure 8. The gradient, F'_I , of the radial velocity component in the inflexion point: (a) as a function of the mass-flow rate \dot{m} , (b) as a function of the velocity F_I at the inflexion point.

and the MW approach. That expresses that roughness stabilizes the Type I mode under both approaches.

The situation is more complex for the Type II mode. It can be seen in figure 9(a) that for the YHP approach the Type II mode is destabilized with increasing roughness, whereas it is stabilized for the MW approach in figure 9(b). Nevertheless, destabilization of Type II, for

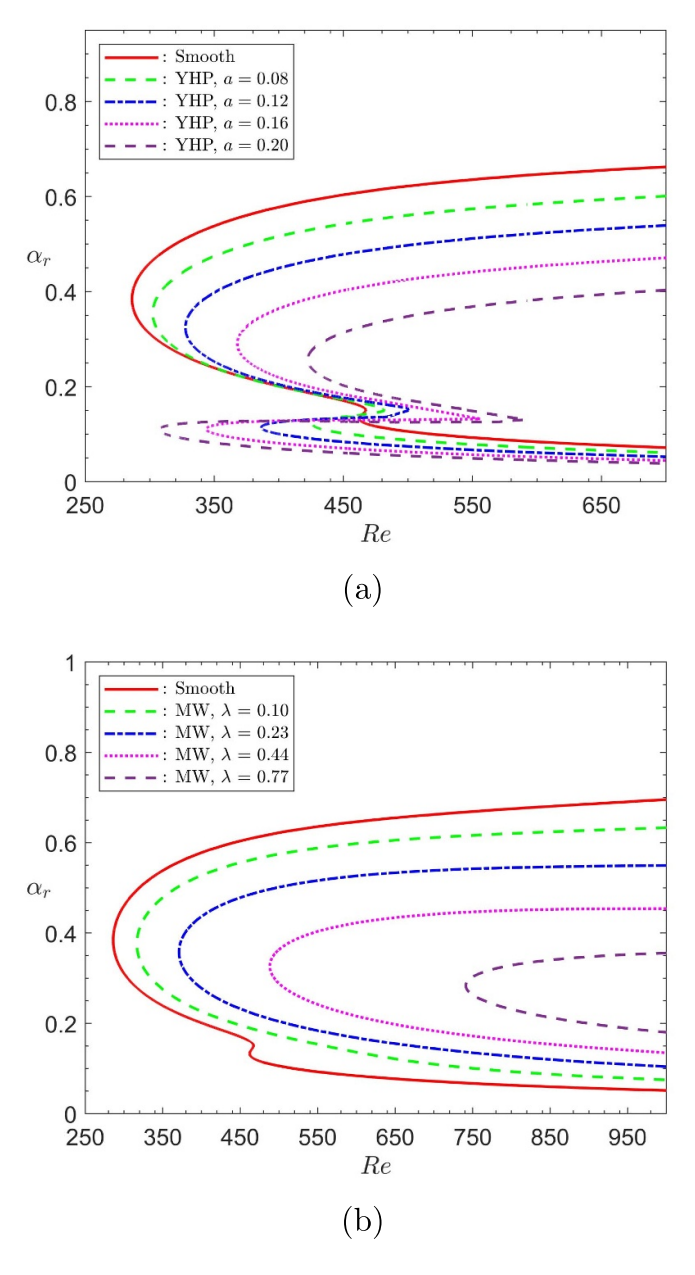


Figure 9. Neutral stability curves displaying the critical wavenumber α_r as a function of the Reynolds number Re: (a) YHP approach, (b) MW approach.

the YHP approach, is not an issue of practical relevance. The growth rates of Type II are substantially smaller than those of Type I (see Cooper *et al* 2015, Garrett *et al* 2016). It is well established that it is the Type I mode that results in the laminar-turbulent transition, and that mode is stabilized for both computational approaches in figure 9.

In section 4.3 it was found that the velocity and location of the inflexion point concurrently display entirely opposing behaviour for both modeling approaches. However, the data in

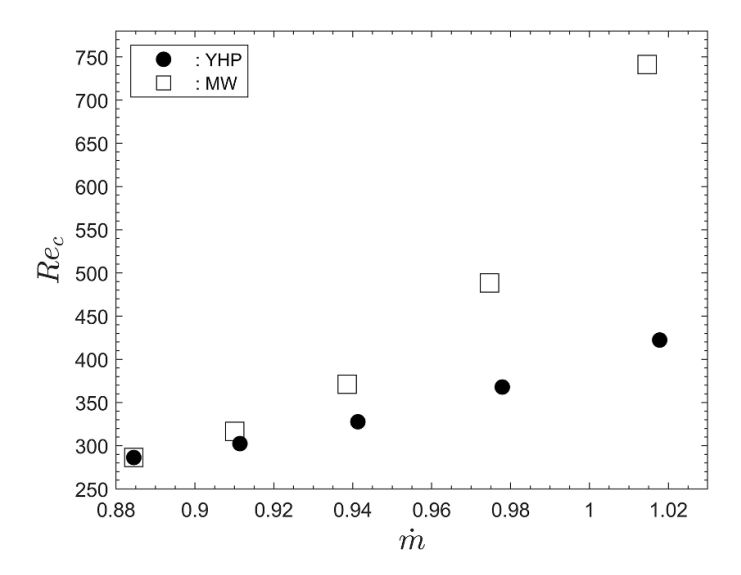


Figure 10. The critical Reynolds number, Re_c , as a function of the roughness level, represented by the mass-flow rate, \dot{m} .

figure 9 show stabilization of Type I, for both computational approaches. This implies, finally, that it is not the characteristics of the inflexion point alone that lead to delayed transition for increasing roughness levels in the two computational approaches. A corresponding comment applies to all other investigated flow characteristics where opposing, or differing, scaling of the data has been found.

The critical Reynolds number Re_c is the lowest value of Re for which a certain disturbance of wavenumber α_r , in figure 9, first becomes unstable. Figure 10 displays the critical Reynolds number, Re_c , for the Type I mode as a function of the mass-flow rate \dot{m} . The figure reveals that Re_c grows significantly faster with \dot{m} for the MW approach than for the YHP approach. That is, the slip factor λ of the MW approach has a substantially larger effect on the stability behaviour of the flow than the amplitude-to-pitch ratio, a, in the YHP approach.

4.5. Number of spiral vortices

Figure 11 depicts the predicted number, n, of spiral vortices along the neutral stability curves, as a function of the Reynolds number, Re. Figure 11(a) reveals that the overall qualitative effect of increasing roughness on the top lobe (Type I) is to shift the lobe toward higher Reynolds numbers, while n decreases. For the MW approach in figure 11(b) it can be seen that the corresponding lobe also moves to higher Re while, in this case, the number of vortices increases.

Figure 12 shows the predicted number n_c of spiral vortices at the critical value Reynolds number, Re_c , for the Type I mode as a function of the mass-flow rate \dot{m} . The figure reveals that the number of vortices remains approximately constant at $n_c = 22$ for the YHP approach for all roughness levels. However, n_c increases sharply with the roughness level for the MW approach.

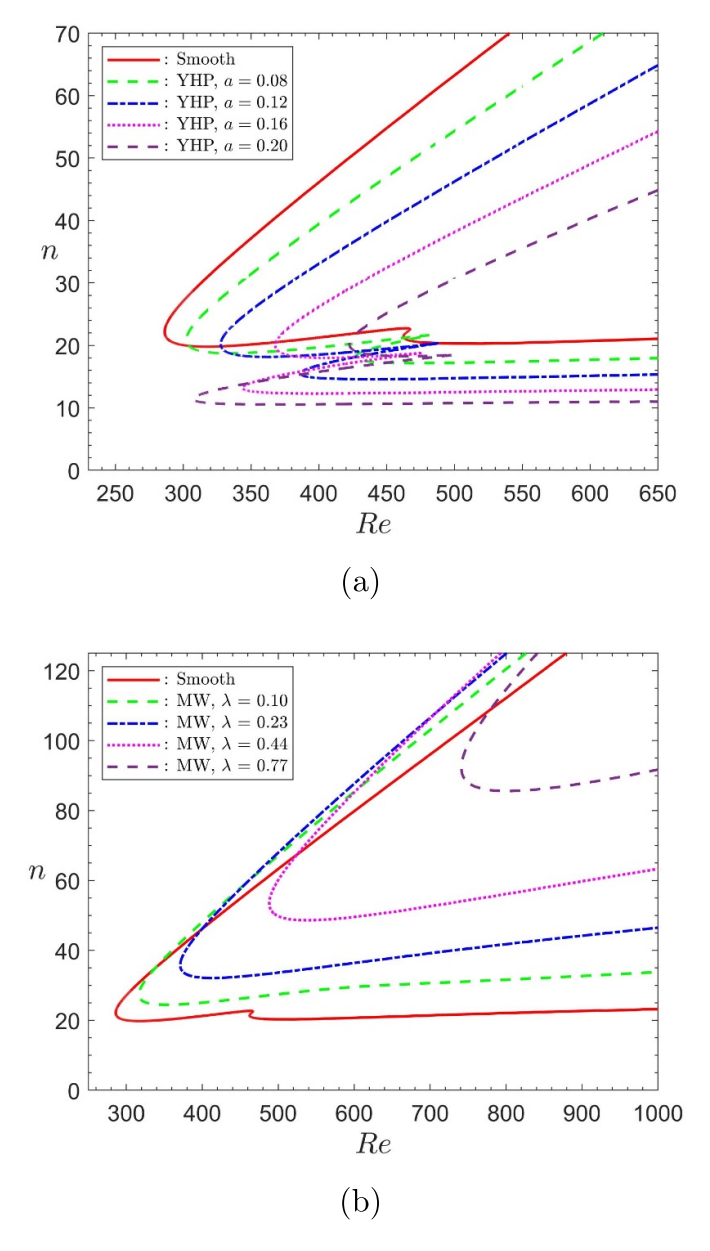


Figure 11. The number of spiral vortices, n, along the neutral stability curves, as a function of the Reynolds number, Re. (a) YHP approach, (b) MW approach.

4.6. Velocity conditions at the disk surface

The value of the azimuthal and the axial velocity component vanish on the surface of the disk under both approaches (cf figures 4–6), and so does the radial velocity component, in the case of the YHP approach. However, with respect to the partial-slip, defined for the MW approach in section 3, the radial velocity F(0) on the disk surface varies here with the roughness level.

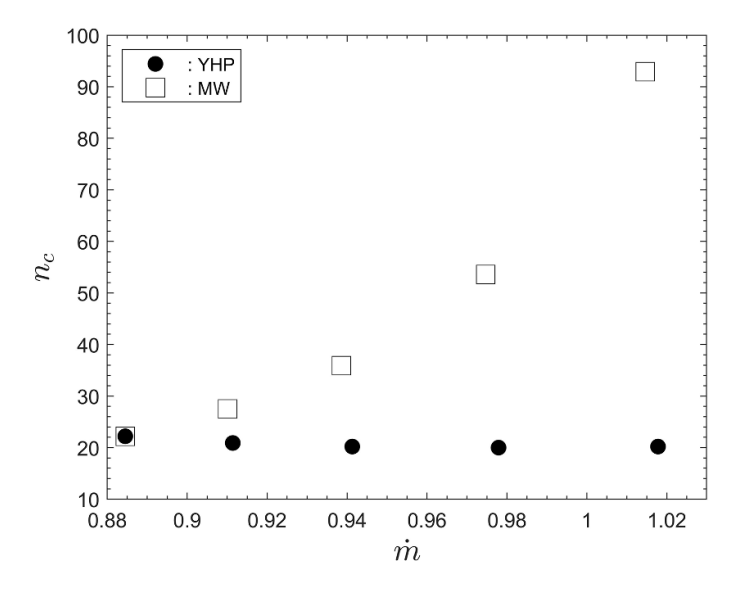


Figure 12. The number, n_c , of spiral vortices, as a function of the critical Reynolds number Re_c for different roughness levels, represented by the mass-flow rates \dot{m} .

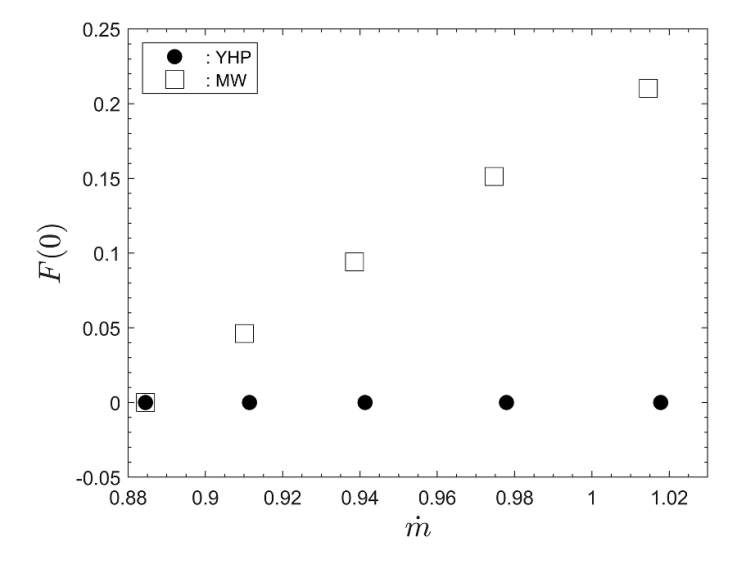


Figure 13. The radial flow velocity on the disk surface, F(0), as a function of the roughness level, represented by the mass-flow rate, \dot{m} .

The non-vanishing radial velocity F(0) for the different roughness levels can be identified in figure 4(b). The relevant numeric data for F(0) are summarized in the rightmost column of table 3 and they are displayed in figure 13 as a function of the roughness level, as represented by the mass-flow rate \dot{m} .

Table 3 also contains the numeric values of the derivatives F'(0), G'(0), H'(0) of the three velocity components at the surface of the disk and these data are displayed in figures 14(a)–(c). Figures 14(b) and (c) show, once again, that the behaviour for the YHP and the MW approach

and the 1111 approach, and the vercenty I (o) on the dish surface for the 1111 approach.								
	YHP	YHP	YHP	MW	MW	MW	MW	
m	F'(0)	G'(0)	H'(0)	F'(0)	G'(0)	H'(0)	F(0)	
0.8845	0.5101	-0.6160	0	0.5102	-0.6159	0	0	
0.9114	0.4437	-0.5661	0	0.4615	-0.6668	-0.0923	0.0461	
0.9413	0.3870	-0.5196	0	0.4089	-0.7183	-0.1881	0.0941	
0.9779	0.3338	-0.4719	0	0.3436	-0.7780	-0.3024	0.1512	
1.0178	0.2887	-0.4277	0	0.2731	-0.8380	-0.4206	0.2103	

Table 3. Velocity derivatives F'(0), G'(0), H'(0) at the surface of the disk for, the YHP and the MW approach, and the velocity F(0) on the disk surface for the MW approach.

is fundamentally different for the azimuthal and the axial flow component. However, for the radial flow component, in figure 14(a), the data from the YHP and the MW approach do indeed agree very closely with each other.

Figure 14(a) has shown that F'(0) decreases essentially linearly with \dot{m} , while the relation between λ and \dot{m} , in figure 2, is also approximately linear. Therefore, $F(0) = \lambda F'(0)$ should also scale approximately linearly with \dot{m} , that is consistent with the data for F(0) for the MW approach in figure 13.

The result from figure 14(a) that the data for the derivative F'(0) from both computational approaches agree with each other represents the only case of the entire data comparison where the YHP and the MW approach yielded data for flow characteristics that show the same overall trend and with closely matching numeric values. Therefore, it appeared likely that the velocity derivative on the disk surface (F'(0)) is potentially closely associated with the origin of the postponed laminar-turbulent transition under both computational approaches.

To test the hypothesis whether the derivative F'(0) is a characteristic with major effects on transition, we synthetically modified the data for $F(\zeta)$ at $\zeta=0$ and in the immediate region above the disk to alter F'. The details of this process are summarized in section 6.4 of Yapa (2023). The synthetically modified base-flow profiles were then subjected to the linear-stability analysis. However, the results obtained were inconclusive. It has been found that the flow is marginally stabilized when F'(0) decreases and marginally destabilized when F'(0) increases. However, the effects were found to be rather weak.

5. Conclusion

Effects of surface roughness on the laminar-turbulent transition of von Kármán boundary-layer flow were discussed. Roughness-modified mean base flow profiles were obtained for the frequently used MW and YHP roughness modeling approaches. The two data sets were obtained by the two codes previously used in the context of Cooper *et al* (2015), Garrett *et al* (2016). Corresponding characteristics of the two sets of roughness-modified mean base flow profiles were analyzed. The two sets of profiles were then subjected to a linear-stability analysis using the same stability code as in Cooper *et al* (2015), Garrett *et al* (2016).

The results obtained for the type of roughness considered here have shown that it is impossible to adjust the roughness-modeling parameters for the MW and the YHP approach such that identical profiles for the three velocity components of the von Kármán boundary-layer are obtained. Thus, it was demonstrated that, in their current form and for the type of roughness considered, the two approaches are not compatible. Nevertheless, for the data from both approaches the linear-stability analysis predicts postponed transition. The only existing option for a direct data comparison between results for the MW and the YHP approach was to

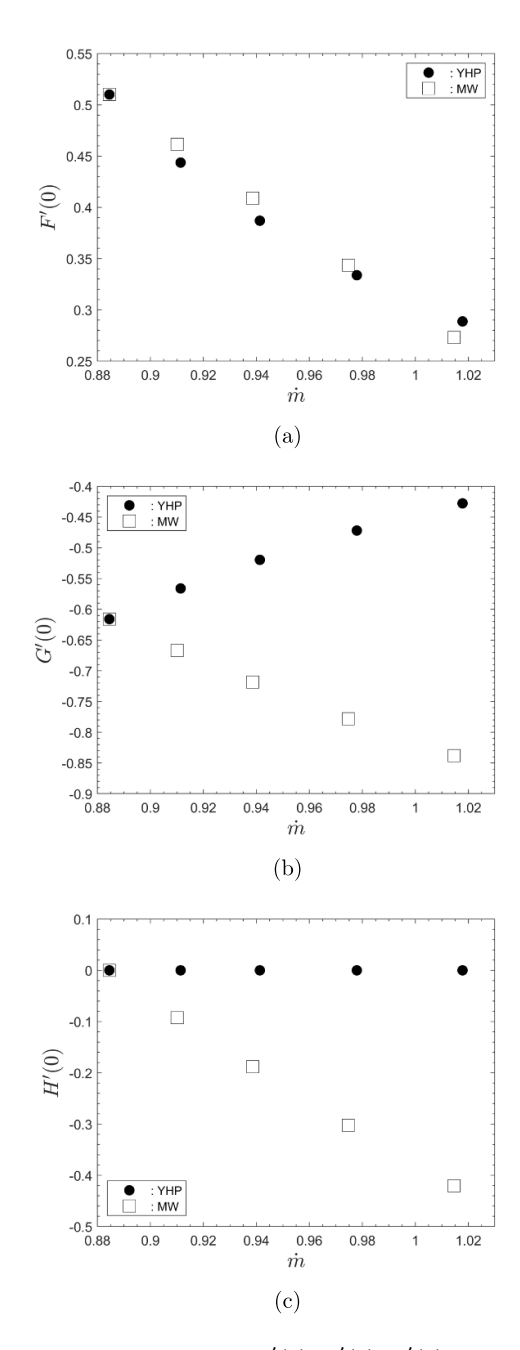


Figure 14. Derivatives F'(0), G'(0), H'(0) of the flow-velocity components at disk surface as a function of the mass-flow rate, \dot{m} .

consider systems as physically equivalent when the volumetric flow rate through the system is equal. While that criterion is somewhat unsatisfactory the main conclusions emerging are independent of it.

The linear-stability code was unaware of which particular set of input modified mean profiles resulted from which one of the two roughness-modeling approaches. The intention was to identify specific characteristics of the roughness-modified mean-flow profiles appearing in the same form for the two sets of profiles. The analysis has shown that such shared data-scaling characteristics do not exist for the most prominent flow-profile characteristics considered. Yet, the final, overall prediction from both approaches is postponed transition.

In Cooper *et al* (2015) we applied partial slip to the base flow but no slip to the linear perturbations. More recently Thomas *et al* (2023) revisited the problem first considered in Cooper *et al* (2015). In this study the authors presented an argument for the adoption of the partial-slip boundary conditions to be applied to the calculation of both the base flow and perturbation quantities. The conclusion that periodic small amplitude roughness proves to be a stabilizing feature remains the case when one considers isotropic roughness (a combination of partial-slip in both the radial and azimuthal directions). However, the predicted boundary layer stabilization was significantly reduced when compared to the findings of Cooper *et al* (2015). Furthermore, in the presence of purely radial partial-slip, the type I mode is instead predicted to be destabilized, a result opposed to the original findings of Garrett *et al* (2016). Nevertheless, the result of Thomas *et al* (2023) do not affect the issue identified herein that the MW and the YHP approach lead to roughness-modified mean base profiles that are not compatible with each other.

Therefore, the main theoretical challenge arising from the current discussion regards the question of which particular characteristics of the roughness-modified mean-flow profiles lead or contribute to the postponed transition. To begin tackling that challenge one could, perhaps, begin by applying methodologies similar to those summarized in Marquet *et al* (2008) which investigates how base-flow modifications alter the stability properties of vortex shedding for flow around cylinders. However, the approach in Marquet *et al* (2008) was developed for two-dimensional flow, whereas the von Kármán boundary layer is fully three-dimensional.

Nevertheless, from an experimentalists perspective the main conclusion is that, ultimately, it is only a laboratory study that could resolve the issues identified by the results discussed here. Experiments would shed light on the question regarding whether the MW or the YHP approach, if either, predicts data for mean-flow profiles in agreement with measurements. Clearly, the opposing data-scaling trends displayed in figures 4–14 imply that at least one of the two approaches must produce results that cannot be in agreement with future experiments.

However, conducting a laboratory study requires a state-of-the-art experimental rotatingdisk facility with the associated measurement technology (i.e. hot-wire system). Such an infrastructure is, unfortunately, currently not available to us, nor does it exist elsewhere in the UK. It will require many years and substantial funds to develop such a facility.

Data availability statement

The data that support the findings are available within the article.

Conflict of interest

The authors have no conflicts of interest to disclose.

Authorship contribution statement

P Y A G S Yapa: Data curation (lead), Formal analysis (equal) Writing of manuscript and proof reading (equal), Methodology (equal). **P** Griffiths: Maintaining and modifying computational codes (equal), Writing of manuscript and proof reading (equal), Methodology (equal). **S** J Garrett: Maintaining and modifying computational codes (equal) Writing of manuscript and proof reading (equal), Methodology (equal). **P** J Thomas: Conceptualization (lead), Writing of manuscript and proof reading (lead), Formal analysis (equal), Methodology (equal).

References

- Al-Malki M A S, Fildes M and Hussain Z 2022 Competing roughness effects on the non-stationary crossflow instability of the bouldary-layer over a rotating broad cone *Phys. Fluids* **34** 104103
- Alfredsson P H, Kato K and Lingwood R J 2024 Flows over rotating disks and cones *Annu. Rev. Fluid Mech.* **65** 45–68
- Alqarni A A, Alveroglu B, Griffiths P T and Garrett S J 2019 The instability of non-Newtonian boundary-layer flow over rough rotating disks *J. Non-Newton. Fluid Mech.* 273 104174
- Alveroglu B 2020 On the mean flow solutions of related rotating disk flows of the BEK system *Fund. J. Math. Appl.* **3** 168–74
- Alveroglu B 2021 On the stability of Ekman boundary-layer flow over a rough disk with a wavy surface profile *Numer. Methods Part. Differ. Equ.* 37 1495–505
- Alveroglu B, Segalini A and Garrett S J 2016 The effect of surface roughness on the convective instability of the BEK family of boundary-layer flows *Eur. J. Mech. B* **56** 178–87
- Cooper A J, Harris J H, Garrett S J, Ozkan M and Thomas P J 2015 The effect of anisotropic and isotropic roughness on the convective stability of the rotating disk boundary layer *Phys. Fluids* 27 014107
- Garrett S J, Cooper A J, Harris J H, Ozkan M, Segalini A and Thomas P J 2016 On the stability of von Karman rotating-disk boundary layers with radial anisotropic roughness *Phys. Fluids* **28** 014104
- Gregory N, Stuart J T and Walker W S 1955 On the stability of three-dimensional boundary layers with application to the flow due to a rotating disk *Phil. Trans. R. Soc. A* **248** 155–99
- Iqra T, Nadeem S, Ghazwani H A, Duraihem F Z and Alzabut J 2024 Instability analysis for MHD boundary layer flow of nanofluid over a rotating disk with anisotropic and isotropic roughness *Heliyon* 10 e26779
- Khan M, Salahuddin T, Altanji M and Khan Q 2022a Calculating the isotropic and anisotropic roughness by using MW model: a variable thermal conductivity study *Radiat. Phys. Chem.* **194** 110010
- Khan M, Salahuddin T, Awais M and Al Awan B 2022b Thermophysical properties of fluid and gases near a solar rough rotating disk *Waves Random Complex Media* **35** 5394–409
- Lingwood R J and Alfredsson P H 2015 Instabilities of the von Kármán boundary layer *Appl. Mech. Rev.* **67** 030803
- Mack L M 1985 The wave pattern produced by point source on a rotating disk AIAA 23rd Aerospace Sciences Meeting (Reno, Nevada) p AIAA-85-0490
- Malik M R 1986 The neutral curve for stationary disturbances in rotating-disk flow *J. Fluid Mech.* **164** 275–87
- Marquet O, Sipp D and Jacquin L 2008 Sensitivity analysis and passive control of cylinder flow *J. Fluid Mech.* **615** 221–52
- Miklavčič M and Wang C Y 2004 The flow due to a rough rotating disk Z. Angew. Math. Phys. 55 235–46
- Navier C L M H 1823 Mémoire sur les lois du mouvement des fluides *Mem. Acad. R. Sci. Inst. France* 6 389–440
- Owen J M and Rogers R H 1989 Flow and Heat Transfer in Rotating-Disc Systems. Vol. 1: Rotor-Stator Systems (Research Studies Press Ltd)
- Thomas C, Alveroglu B, Stephen S O, Al-Maki M A S and Hussain Z 2023 Effect of slip on the linear stability of the rotating disk boundary layer *Phys. Fluids* **35** 084118

- Thomas C, Stephen S O and Davies C 2020 Effect of partial slip on the local-global linear stability of the infinite rotating disk boundary layer *Phys. Fluids* **32** 074105
- von Kármán T V 1921 Über laminare und turbulente Reibung ZAMM—J. Appl. Math. Mech./Z. Angew. Math. Mech. 1 233–52
- Wimmer M 1988 Viscous flows and instabilities near rotating bodies *Prog. Aerosp. Sci.* **25** 43–103 Yapa P Y A G S 2023 Designing optimal roughness: a theory-led approach to roughness-based drag reduction *PhD Thesis* School of Engineering, University of Warwick (available at: wrap.warwick.ac.uk/id/eprint/187476/)
- Yoon M S, Hyun J M and Park J S 2007 Flow and heat transfer over a rotating disk with surface roughness *Int. J. Heat Fluid Flow* **28** 262–7